JOURNAL OF COMPUTATIONAL PHYSICS 42, 108–123 (1981)

One-Dimensional Compressible Gas Dynamics Calculations Using the Boltzmann Equation

ROLF D. REITZ

Department of Mechanical and Aerospace Engineering, Princeton University, Princeton, New Jersey 08544

Received August 14, 1980

One-dimensional inviscid gas dynamics computations are made using a new method to solve the Boltzmann equation. The numerical method is explicit and is based on concepts from the kinetic theory of gases. The gas density, velocity and temperature are computed by integrating numerically the molecular velocity distribution function. This in turn is computed from the Boltzmann equation using an operator splitting approach. The basic algorithm is shown to be efficient and unconditionally stable. The method is tested for a single component diatomic ideal gas on initial-boundary value problems. These include the Riemann shock-tube problem and shock wave reflection from a stationary wall for a range of incident Mach numbers up to $M = 10$. The results show that the method can offer significant advantages over standard finite difference methods for certain problems. Shock waves are resolved well with minimal oscillations in the solution, and accurate results are obtained with Courant numbers an order of magnitude larger than the usual stability limit. The method performs best in regions of the flow which are close to thermodynamic equilibrium and is first order accurate in regions which are far from equilibrium, as would be predicted from kinetic theory arguments.

INTRODUCTION

Recently several numerical methods have been proposed which use Boltzmann-like equations as the starting point for the computation of inviscid compressible gas dynamics. A velocity distribution function is chosen as the dependent variable and the flow variables (gas temperature, density and velocity) are computed from moments of the distribution function over molecular velocity space.

Kaniel and Falcovitz [2] proposed a transport model for isentropic gas dynamics. In their work an auxiliary thermodynamic distribution function was defined and this was used to yield the macroscopic flow variables via moment relations. This distribution function could be integrated analytically in certain special cases, but its second order moment differs from that of the true molecular velocity distribution function whose evolution is governed by the Boltzmann equation. Pullin [1] investigated both deterministic and Monte Carlo methods for the solution of gas dynamics problems using the Boltzmann equation. With the Monte Carlo method the velocity distribution function also included the contributions made by an ensemble of individual discrete particles. Their initial distribution corresponded to a Maxwellian

0021-9991/81/070108-16$02.00/0

distribution and they were tracked during the computation. In his deterministic method the solution variables were found from analytically computed fluxes from one cell to the next, using the Maxwellian distribution function in the solution algorithm.

In this paper we formulate and apply a method which parallels the kinetic theory of gases more closely. The Boltzmann equation is solved deterministically using an operator splitting technique which is valid in the thermodynamic equilibrium limit, and the Maxwellian equilibrium velocity distribution function is also used in the solution algorithm. A feature of the present method is to allow the possibility of long range communication between computational cells and no numerical differentiation is required. The method is explicit and is shown to be efficient and unconditionally stable.

We consider one-dimensional flows of a single component diatomic ideal gas and neglect body forces. In this case the usual equations of inviscid gas dynamics may be written as [3]

$$\frac{\partial}{\partial t}\rho + \frac{\partial}{\partial x}(\rho u) = 0, \tag{1}$$

$$\frac{\partial}{\partial t}(\rho u) + \frac{\partial}{\partial x}(\rho u^2 + P) = 0, \tag{2}$$

$$\frac{\partial}{\partial t}(\rho E) + \frac{\partial}{\partial x}[u(\rho E + P)] = 0, \tag{3}$$

where ρ is the gas density, u is the gas velocity, P is the pressure and E is the total energy per unit mass, i.e.,

$$E = c_v T + e_i + \tfrac{1}{2}u^2. \tag{4}$$

Here e_i is the molecular internal energy and $c_v T$ is the molecular translation kinetic energy per unit mass. Equations (1), (2) and (3) are supplemented by the equation of state

$$P = \rho R T, \tag{5}$$

where R is the gas constant and T is the temperature.

The Boltzmann equation, as applied in the kinetic theory of gases, is [3]

$$\frac{\partial f}{\partial t} + c\frac{\partial f}{\partial x} = \frac{\delta f}{\delta t}\bigg)_{\text{coll}}. \tag{6}$$

$f(x, c, t)$ is the probability density of molecular velocities in the phase space ranges dc about c and dx about x at time t. $\delta f/\delta t)_{\text{coll}}$ is the contribution to the evolution of the velocity distribution function due to molecular collisions.

The thermodynamic equilibrium solution to the Boltzmann equation is obtained in the limit

$$\left.\frac{\delta f}{\delta t}\right)_{\text{coll}} = 0.$$

This states that, locally, each depleting molecular collision is balanced by a corresponding replenishing collision. In this case the inviscid thermodynamic equilibrium solution is the one-dimensional Maxwellian distribution

$$f_0(x, c, t) = f_0(\rho, u, T; c) = \frac{\rho}{\sqrt{2\pi RT}} e^{-(c-u)^2/2RT}. \tag{7}$$

The conservation laws, Eqs. (1), (2) and (3) can be derived from Eq. (6) with the definitions

$$\rho = \int_{-\infty}^{\infty} f\,dc, \tag{8}$$

$$\rho u = \int_{-\infty}^{\infty} cf\,dc, \tag{9}$$

$$\rho E = \int_{-\infty}^{\infty} \left(\frac{c^2}{2} + e_i\right) f\,dc$$

$$= \frac{5}{2}\rho RT + \frac{1}{2}\rho u^2 \tag{10}$$

and

$$\int_{-\infty}^{\infty} \psi \left.\frac{\delta f}{\delta t}\right)_{\text{coll}} dc = 0 \qquad \text{for } \psi = 1, c, \left(\frac{c^2}{2} + e_i\right).$$

The last equation expresses overall conservation of mass, momentum and energy. Notice that, for one-dimensional gas motion, the translational kinetic energy in Eq. (4), $c_v T$, is $RT/2$; the contributions due to remaining translational degrees of freedom (not considered in a one-dimensional model) are absorbed into the molecular internal energy, e_i.

Numerical Method

The solution variables $\rho(x, t)$, $u(x, t)$ and $T(x, t)$ were computed explicitly from solutions of the Boltzmann equation (6), and from the moment equations (8), (9) and (10). ρ_j^n, u_j^n and T_j^n are the corresponding numerical approximations to the continuous variables and they were defined for simplicity on an equally spaced mesh at grid

points $x_j = j\Delta x$ at time $t = n\Delta t$, where $j = 1,..., N$; Δx is the mesh spacing, Δt is the numerical time step and N is the number of grid points in the physical space.

The molecular velocity distribution function $f(x, c, t)$ was approximated by the function $f^n_{j,l} = f(j\Delta x, l\Delta c_j, n\Delta t)$, where $l = -L,..., 0,..., L$; $2L + 1$ is the number of lattice points in the molecular velocity space and Δc_j is the molecular velocity grid spacing at the points x_j (i.e., an equally spaced net at each x_j).

The Boltzmann equation was solved using operator splitting. Equation (6) was approximated by the pair of equations

$$\left(\frac{\delta f}{\delta t}\right)_{\text{coll}} = 0 \tag{11}$$

and

$$\frac{\partial f}{\partial t} + c\frac{\partial f}{\partial x} = 0. \tag{12}$$

Equation (11) is the statement of thermodynamic equilibrium and its solution is

$$f(x_j, c_l, n\Delta t) = f_0(\rho^n_j, u^n_j, T^n_j; c_l), \tag{13}$$

where f_0 was defined in Eq. (7). Equation (12) represents collisionless molecular transport in the phase space and it defines a mean free path for each molecular velocity. Its solution is

$$f(x_j, c_l, (n+1)\Delta t) = f(x_j - c_l\Delta t, c_l, n\Delta t). \tag{14}$$

This is the exact (discretized) solution to Eq. (12) and no interpolation is required if the velocity grid spacing is chosen such that

$$\Delta c_j = \Delta c = \Delta x/\Delta t. \tag{15}$$

Notice however that for $\Delta t \to 0$, Δx must be decreased correspondingly for Δc to remain bounded. In some studies Δc was chosen independently of Δx and Δt and the solution variables at the points $x_j - c_l\Delta t$ in Eq. (14) were obtained by second order accurate interpolation.

The distribution function does not need to be stored during the computations. Equations (13) and (14) can be combined with Eqs. (8), (9) and (10) to give the algorithm

$$\begin{aligned}
\rho^{n+1}_j &= \sum_{l=-L}^{L} f^{n+1}_{j,l}\Delta c_j, \\
u^{n+1}_j &= \frac{1}{\rho^{n+1}_j}\sum_{l=-L}^{L} l\Delta c_j f^{n+1}_{j,l}\Delta c_j, \\
T^{n+1}_j &= \left[\frac{1}{\rho^{n+1}_j}\sum_{l=-L}^{L}\left(\frac{l^2\Delta c_j^2}{2} + e^*_l\right) f^{n+1}_{j,l}\Delta c_j - (u^{n+1}_j)^2/2\right] \Big/ 2.5R,
\end{aligned} \tag{16}$$

where

$$f_{j,l}^{n+1} = f_0(\rho^n(x_j - c_l\Delta t), u^n(x_j - c_l\Delta t), T^n(x_j - c_l\Delta t); c_l) \tag{17}$$

and

$$e_l^* = 2RT^n(x_j - c_l\Delta t). \tag{18}$$

Equation (18) states that molecules transport their internal energy during the shift in phase space which is governed by Eq. (12).

Unconditional linear stability can be shown using a von Neumann stability analysis of the method for the case where the mesh is defined with Eq. (15). In the analysis Eq. (17) is linearized about the constant state $\bar{\rho}$, $\bar{u}$, $\bar{T}$ with $\rho^n = \bar{\rho} + \underset{\sim}{\rho}$ for example. Writing the Fourier decomposition of the fluctuating part of the solution variables as $\underset{\sim}{\rho}^n = U_{(1)}^n e^{i\Theta}$, $\underset{\sim}{u}^n = U_{(2)}^n e^{i\Theta}$ and $\underset{\sim}{T}^n = U_{(3)}^n e^{i\Theta}$, where $\Theta = jk_x\Delta x$, and replacing the summations in Eqs. (16) by integrations, gives

$$U_{(i)}^{n+1} = GU_{(i)}^n, \tag{19}$$

where the amplification matrix is given in Appendix A. The eigenvalues of the matrix are of the form

$$\lambda^{(i)} = e^{-[k_x^2\Delta t^2(R\bar{T}/2) + i\bar{u}k_x\Delta t]}Q^{(i)},$$

where the $Q^{(i)}$ are functions of RT and $k_x\Delta t$ and are independent of $\bar{u}$. To second order

$$Q^{(i)} = 1, 1 \pm ik_x\Delta ta - a^2k_k^2(\Delta t^2/2),$$

where a is the sound speed $(7RT/5)^{1/2}$. The analysis in Appendix A shows that $|\lambda^{(i)}\bar{\lambda}^{(i)}| \leqslant 1$.

The boundary conditions were computed as follows: For boundaries at the points x_1 and x_N, $f_{j,l}^{n+1}$ was given by Eq. (17) for $x_1 \leqslant x_j - c_l\Delta t \leqslant x_N$ and by

$$f_{j,l}^{n+1} = f_0(\rho_m^n, u_m^n, T_m^n; c_l), \tag{20a}$$

where $m = 1$ for $x_j - c_l\Delta t < x_1$, and $m = N$ for $x_j - c_l\Delta t > x_N$. Equation (20a) specifies Neumann boundary conditions since it implies zero gradients in the solution variables outside of the computational domain. For the shock reflection studies to be presented in the next section Eq. (20a) was applied with u_m^n specified equal to zero at the wall, i.e., for $m = N$. A specular reflection boundary condition was also explored for comparison. Here the boundary condition was instead

$$f_{j,l}^{n+1} = f_0(\rho^n(x_j - |c_l|\Delta t), -u^n(x_j - |c_l|\Delta t), T^n(x_j - |c_l|\Delta t); c_l) \tag{20b}$$

for $x_j - c_l\Delta t > x_N$. Finally, for a moving internal boundary situated between x_B and x_{B+1}, transport of mass across the boundary was prevented by applying Eq. (20a) at the point x_B (with $m = B$) for $x_j - c_l\Delta t > x_B$ and similarly at x_{B+1} (with $m = B + 1$) for $x_j - c_l\Delta t < x_{B+1}$.

Discussion of Results

The method in Eqs. (16) was applied to two different initial-boundary value problems and the results are shown in Tables I to IV and in Figs. 1 to 5. The figures show computed non-dimensional density, temperature, velocity and pressure profiles in the physical domain $0 \leqslant x \leqslant 1$. The solid lines show the exact solution. The physical mesh spacing was $\Delta x = 0.01$ and the non-dimensional gas constant was chosen as $R = 2.667 \times 10^{-3}$ in all cases.

Figures 1 and 2 show computational results of the Riemann shock-tube test problem which was studied in detail in Sod [4]. In this problem a diaphragm separates two regions, each in a constant state at $t = 0$, with $\rho = 1$, $T = 375$, $u = 0$ for $0 \leqslant x \leqslant 0.5$ and $\rho = 0.125$, $T = 300$, $u = 0$ for $0.5 < x \leqslant 1$. The figures show details of the flow field 32 cycles after the diaphragm is removed.

The molecular velocity grid spacing was chosen independently of Δx and Δt (cf. Eq. (15)) with

$$\Delta c_j = (1.75RT_j^n)^{1/2}. \tag{21}$$

The time step Δt was 0.005 and $2L + 1$, the number of grid points in molecular velocity space, was 11. The CDC 6600 execution time per step was about 0.20 sec. This compares favorably with the 0.22 to 0.36 sec. of the finite difference methods which are compared in Sod [4].

The results in Figs. 1 and 2 correspond to a maximum Courant number $(|u| + a)\Delta t/\Delta x \simeq 1.1$. The shock wave at $x = 0.78$ is seen to be located accurately and the wave is resolved within two to three zones. There is a slight undershoot at its downstream side. In Fig. 1 the contact discontinuity at $x \simeq 0.65$ has been smeared and it contains 8–10 grid points. The pressure is almost constant actross the contact

TABLE I

Wall and Post-shock Pressure, Density and Temperature for Reflected $M = 2$ Shock Waves with 41 and 11 Grid Points in Molecular Velocity Space

		$\Delta c = 0.85,\ 2L + 1 = 41$				$\Delta c_j = (1.75RT_j)^{1/2},$ $2L + 1 = 11$	
		$\Delta t = 0.0118$[a]		$\Delta t = 0.0025$[b]		$\Delta t = 0.0025$	
	Exact	Wall	Post-shock	Wall	Post-shock	Wall	Post-shock
P	1.0356	1.0361	1.0296	1.0357	1.0359	1.0401	1.0401
ρ	0.1290	0.1318	0.1283	0.1308	0.1286	0.1332	0.1301
T	3020.1	2948.4	3008.6	2969.2	3020.6	2928.3	2997.0

[a] Figure 3.
[b] Figure 4.

TABLE II

Wall and Post-shock Pressure, Density and Temperature at $t = 0.32$ for Reflected $M = 6$ Shock Waves with B.C.'s Eqs. (20a and b)[a]

		Neumann B.C. Eq. (20a)		Specular reflec. B.C. Eq. (20b)	
	Exact	Wall	Post-shock	Wall	Post-shock
P	2.1671	2.1661	2.1721	2.1661	2.1720
ρ	0.1888	0.1992	0.1889	0.1927	0.1888
T	4307.7	4078.0	4312.2	4215.5	4312.5

[a] $\Delta c = 0.85$, $2L + 1 = 41$, $\Delta t = 0.0025$.

TABLE III

Wall and Post-shock Pressure, Density and Temperature at $t = 0.32$ for Reflected $M = 10$ Shock Waves with B.C.'s Eqs. (20a and b)[a]

		Neumann B.C. Eq. (20a)		Specular reflec. B.C. Eq. (20b)	
	Exact	Wall	Post-shock	Wall	Post-shock
P	2.3611	2.3614	2.3610	2.3620	2.3613
ρ	0.1958	0.2049	0.1958	0.1950	0.1959
T	4521.8	4215.5	4521.1	4543.3	4520.3

[a] $\Delta c = 0.85$, $2L + 1 = 41$, $\Delta t = 0.005$.

TABLE IV

Wall and Post-shock Pressure, Density and Temperature at $t = 0.376$ for Reflected $M = 10$ Shock Wave with Chapman–Enskog Correction[a]

		$\alpha = 0$		$\alpha = 0.6 \times 10^{-4}$		$\alpha = 2.4 \times 10^{-4}$	
	Exact	Wall	Post-shock	Wall	Post-shock	Wall	Post-shock
P	2.3611	2.3643	2.3421	2.3589	2.3365	2.3437	2.3224
ρ	0.1958	0.2054	0.1954	0.2017	0.1937	0.2137	0.1898
T	4521.8	4316.9	4495.4	4386.1	4523.8	4112.5	4588.3

[a] B.C. Eq. (20a), $\Delta c = 0.85$, $2L + 1 = 41$, $\Delta t = 0.0118$.

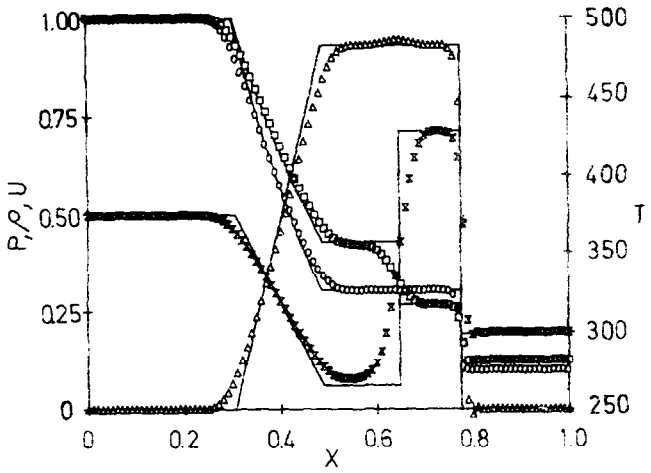

FIG. 1. Computed profiles of pressure (○), density (□), velocity (△) and temperature (⧖)for Riemann shock-tube problem at $t = 0.16$. $\Delta t = 0.005$, $2L + 1 = 11$. $\Delta c = (1.75RT)^{1/2}$. (——) Exact solution.

but there is a slight bulge in the velocity profile in this region. The end points of the rarefaction wave have been rounded.

A comparison with the results of the methods tested in Sod [4] shows that the resolution of the shock wave in Figs. 1 and 2 is better than that of the second order accurate Lax Wendroff and MacCormack methods which had four to six zones and noticeable oscillatory overshoots. In the region of the contact discontinuity, the results in Fig. 1 are comparable to those of the first order accurate Godunov scheme which had seven to eight zones in the contact but had five to six zones in the shock.

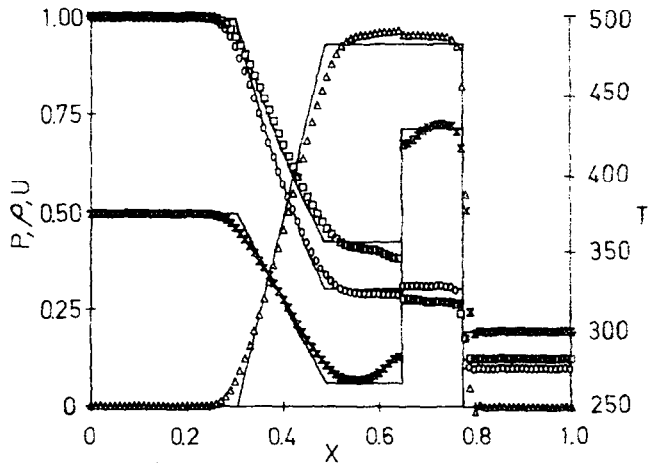

FIG. 2. Computed profiles of pressure (○), density (□), velocity (△) and temperature (⧖) for Riemann shock-tube problem at $t = 0.16$ treating contact discontinuity as a moving internal boundary. $\Delta t = 0.005$, $2L + 1 = 11$, $\Delta c = (1.75RT)^{1/2}$. (——) Exact solution.

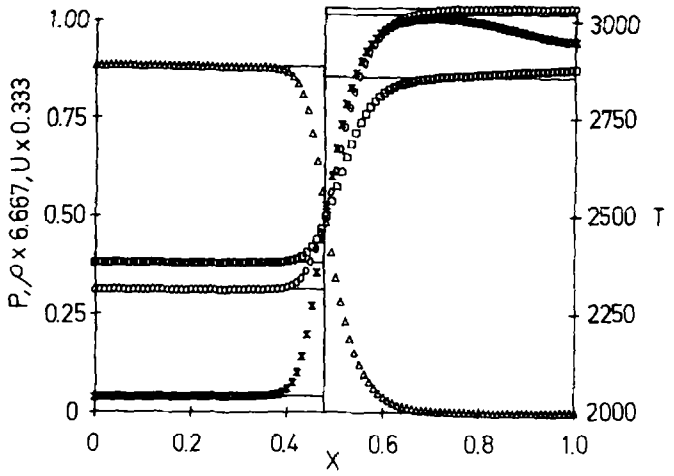

FIG. 3. Computed profiles of pressure (○), density (□), velocity (△) and temperature (X), at $t = 0.376$ for $M = 2$ incident shock wave reflected from wall at $x = 1$. $\Delta t = 0.0118$, $2L + 1 = 41$, $\Delta c = 0.85$. (——) Exact solution.

The resolution of the contact discontinuity is improved in the results which are shown in Fig. 2. Here the contact was treated as a moving internal boundary using a capturing and tracking approach. The contact was captured at the point in the flow field where the conditions: $|\partial T/\partial x|$ is a local maximum and $|\partial P/\partial x|$ and $|\partial u/\partial x|$ are less than ε (=1.5), were satisfied. It was tracked by moving the boundary in steps such that $x_B^{n+1} = x_B^n + u_B^n \Delta t$. Figure 2 shows that the contact discontinuity is represented well with this approach. There are, however, small jumps in the pressure and the velocity across the contact whose magnitude was found to be influenced by

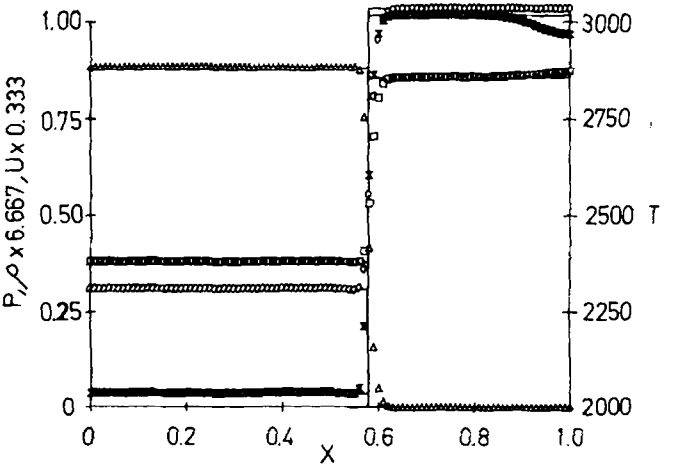

FIG. 4. Computed profiles of pressure (○), density (□), velocity (△) and temperature (X) at $t = 0.32$ for $M = 2$ incident shock wave reflected from wall at $x = 1$. B.C. Eq. (20a), $\Delta t = 0.0025$, $2L + 1 = 41$, $\Delta c = 0.85$. (——) Exact solution.

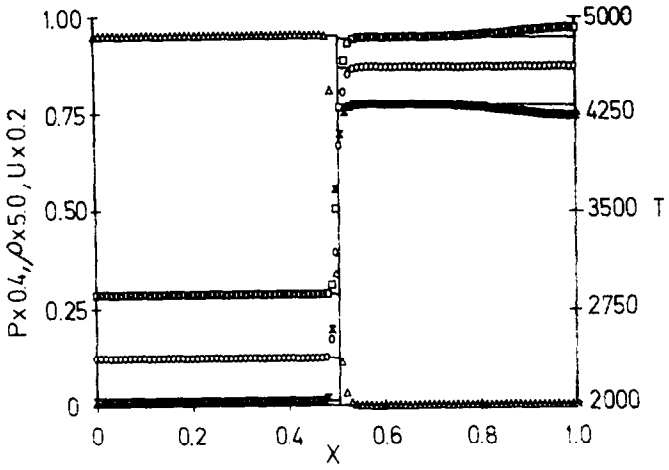

FIG. 5. Computed profiles of pressure (○), density (□), velocity (△) and temperature (X) at $t = 0.32$ for $M = 6$ incident shock wave reflected from wall at $x = 1$ using specular reflection B.C. Eq. (20b). $\Delta t = 0.0025$, $2L + 1 = 41$, $\Delta c = 0.85$. (——) Exact solution.

the choice of ε. The rounded head and tail regions of the density and temperature profiles survived from the time that the contact was captured. These regions sharpened gradually in such a way that the solution approached a step discontinuity at later times (not shown in the figure).

Figures 3, 4 and 5 and the data in Tables I to IV summarize computations of shock wave reflection from a stationary wall. In each case an incident shock was reflected from the wall at $x = 1$ and the boundary conditions were given by Eqs. (20). The initial data were prescribed as a step change in the solution variables at $x = 0.5$ with the jump given by the exact solution for the incident shock wave. The computations used $\Delta c = 0.85$ and $2L + 1 = 41$ unless otherwise noted. The execution time was found to increase roughly linearly with $2L + 1$.

Figures 3 and 4 show details of the reflected shock for $M = 2$ incident shock waves using the Neumann boundary condition Eq. (20a). The shock location is seen to be computed accurately. For the results in Fig. 3 the timestep was such that Eq. (15) was satisfied and the results correspond to a maximum Courant number of 6.37. The reflected wave is smeared over 16–17 zones. In Fig. 4 the timestep was chosen as $t = 0.0025$; thus interpolation was required in the solution algorithm. The maximum Courant number was 1.37 and the shock is now resolved within 3–4 zones.

The smearing of the shock wave in Fig. 3 (and the contact discontinuity in Fig. 1) can be explained by using arguments from kinetic theory. In kinetic theory the average distance traveled by molecules between collisions, the mean free path, is proportional to at^*, where a is a characteristic molecular velocity (taken as the sound speed) and t^* is a characteristic time between collisions. For small departures from equilibrium, the non-equilibrium diffusion coefficient is proportional to the product of

the characteristic molecular velocity and the relaxation length (the mean free path) [5, p. 370], i.e.,

$$D = \beta_1 a^2 t^* = \beta R T t^*, \tag{22}$$

where D is a diffusion coefficient and the β are constants of order 1. The inter-collision time t^* is, in general, a function of the molecular collision cross-section, number density and molecular velocity. However, in the construction of the present numerical method t^* is by definition equal to Δt. This is because the operator splitting in Eqs. (11) and (12) allows collisional equilibration to occur only once each timestep.

Indeed a comparison of the relative thickness of the shock waves in Figs. 3 and 4 shows agreement with Eq. (22) since the theoretical wave thickness is proportional to D [3], and the thickness differs by a factor of 4.7 for the two waves as does the timesteps used. This indicates that the method is first order accurate in regions which are far from thermodynamic equilibrium.

The data in Table I show the computed pressure, density and temperature at the wall and immediately behind the reflected shock (at the point of maximum temperature) for the results in Figs. 3 and 4. The wall values of the flow variables agree with the exact solution in the theoretically uniform region behind the reflected shock to within 2.4 and 1.7%, respectively. The results in the third section of Table I show the effect on accuracy of a coarse grid in molecular velocity space. In this case $2L + 1 = 11$ and the variable velocity grid spacing (Eq. (21)) differs by a factor of about 4 from that used for the results in Figs. 3 and 4. The error in the computed temperature at the wall can be seen to be still only about 3%.

In Table I the wall pressure is seen to be computed accurately but the density and temperature are over- and underestimated, respectively. This differs from the trend reported by Srinivas *et al.* [6] for first order finite difference methods which underestimated the density and overestimated the temperature, but by roughly errors of the same magnitude. The data presented in Tables II and III show that the wall error is influenced by the choice of boundary condition (B.C.) in the present method. In Table II results are given for $M = 6$ incident shock waves ($\Delta t = 0.0025$, maximum Courant number 1.9). For the Neumann B.C. Eq. (20a) the error in the wall temperature is about 5.3% while for the specular reflection B.C. Eq. (20b) the results have errors of about 2.1%.

Details of the reflected wave corresponding to the $M = 6$ incident shock with specular reflection boundary conditions are shown in Fig. 5. The shock is seen to be slightly thinner than that in Fig. 4 ($M = 2$) and is resolved within two to three points. Its location is computed accurately. With increases in the shock Mach number the wave thickness decreased even further and too few zones within the wave eventually resulted in negative temperatures being computed ahead of the incident shock. This was found to be due to the second order accurate interpolation in the solution algorithm; first order interpolation broadened the shock such that this was avoided. In the results to be presented next the problem was remedied instead by increasing Δt (and hence, the shock thickness (cf. Eq. (22))) and by adding an additional intermediate point to the temperature step initial data.

Tables III and IV show results for $M = 10$ incident shock waves. In this problem the wall pressure increases by three orders of magnitude during the reflection process. The results in Table III ($\Delta t = 0.005$, maximum Courant number 3.9) again show that improved accuracy is obtained with the specular reflection boundary condition Eq. (20b). The wall temperature error is about 6.8% using Eq. (20a) and is less than 1% using the specular reflection condition Eq. (20b). Notice in this case that the wall temperature and density are now overestimated and underestimated, respectively. (Post-shock values now correspond to point of maximum density.) The improvements in accuracy which are seen in Tables II and III may be due to the fact that mass and energy are properly conserved at the wall with the use of the specular reflection boundary conditions, Eq. (20b).

The results in the $\alpha = 0$ columns of Table IV show the effect of an increased timestep for the $M = 10$ incident wave. Here $\Delta t = 0.0118$ (i.e., no interpolation is required in the solution algorithm and the maximum Courant number is 9.2) and the boundary condition was given by Eq. (20a). The computed temperature at the wall is seen to agree with the exact solution to within 4.5% which is a slight improvement over the corresponding Neumann boundary condition case in Table III. The reflected shock in Tables III and IV were resolved within 4–5 and 16–18 zones respectively, which is also in agreement with the prediction of Eq. (22).

The remaining entries in Table IV show an attempt to account for non-equilibrium diffusional effects by using the Chapman–Enskog correction to the molecular distribution function (written for one-dimensional gas flows). The right hand side of Eq. (17) was multiplied by the factor $1 + \psi^n_{j,l}$, where

$$\psi^n_{j,l} = -\alpha \left\{ \frac{(c_l - u^n_j)}{T^n_j} \left[\frac{(c_l - u^n_j)^2}{2RT^n_j} - \frac{3}{2} \right] \frac{T^n_{j+1} - T^n_j}{\Delta x} + \frac{4}{5} \left[\frac{(c_l - u^n_j)^2}{RT^n_j} - 1 \right] \frac{(u^n_{j+1} - u^n_j)}{\Delta x} \right\}. \tag{23}$$

In kinetic theory the parameter α in Eq. (23) is a local relaxation time which is related to the viscosity and the thermal conductivity of the gas [3]. It was regarded as a free parameter for the results in Table IV.

A comparison between the results in Table IV shows that the correction improves the accuracy of the computed temperatures by about 1.5% for $\alpha = 0.6 \times 10^{-4}$. However, the reflected shock thickness was sensibly unchanged. Larger values of α are seen in Table IV to lead to inaccurate results for both the wall values and for the reflected shock jump conditions (and shock speed), and negative temperatures resulted for $\alpha \gtrsim 3 \times 10^{-4}$.

The fact that the correction in Eq. (23) has a modest effect on the details of the solution could be due to the fact that it strictly only applies for small Knudsen number (ratio of molecular mean free path to a characteristic length, such as the shock thickness). In the present computations a representative Knudsen number is proportional to $\Delta t \Delta c / \Delta x$ which is of order 1 (cf. Eq. (15)).

Conclusions

The results demonstrate that the method presented here can offer significant advantages over standard finite difference methods for the solution of certain gas dynamics problems. The method is explicit and unconditionally stable and allows shock waves to be resolved well with minimal oscillations in the solution. The results show that accurate computations can be made with Courant numbers an order of magnitude larger than the usual stability limit. The efficiency of the method is competitive with that of other methods as is seen by a comparison of computer times for the test problem of Sod [4]. No numerical differentiation is required in the solution algorithm and the treatment of a variety of boundary conditions is shown to be relatively simple.

Numerical diffusion arises naturally in the method; the scheme is first order accurate in regions which are far from thermodynamic equilibrium. This would be predicted from kinetic theory arguments, which also predict that the magnitude of the numerical diffusion exceeds that of the physical diffusion by the product of the timestep and the true molecular collision rate. The results show that this diffusion can be made sufficiently large for shocks to be resolved without recourse to other artificial diffusion mechanisms.

The inherent disadvantage is that the magnitude of the numerical diffusion only approaches that of the physical diffusion for timesteps of the order of the true molecular inter-collision time. For this reason the method could be expected to be most useful for problems whose solution is insensitive to molecular diffusional effects. In this connection it is suggested that further study should include the development of a Chapman–Enskog-type correction which is valid for Knudsen numbers of order 1. The method is being applied to the study of detonation waves and is being tested for multidimensional inviscid gas dynamics computations.

APPENDIX A: Linear Stability Analysis

The amplification matrix in Eq. (19) is given by

$$G = e^{-i\xi}\begin{bmatrix} 1 & -ik_x\Delta t\bar{\rho} & -\bar{\rho}Rk_x^2\dfrac{\Delta t^2}{2} \\ -ik_x\dfrac{\Delta t}{\bar{\rho}}R\bar{T} & 1-k_x^2\Delta t^2R\bar{T} & -ik_x\Delta tR+ik_x^3\dfrac{\Delta t^3R^2\bar{T}}{2} \\ -k_x^2\dfrac{\Delta t^2R\bar{T}^2}{5\bar{\rho}} & -\dfrac{2}{5}ik_x\Delta t\bar{T}+ik_x^3\dfrac{\Delta t^3R\bar{T}^2}{5} & 1-\dfrac{2}{5}k_x^2\Delta t^2R\bar{T}+k_x^4\dfrac{\Delta t^4R^2\bar{T}^2}{10} \end{bmatrix},$$

where $\xi = k_x^2 \Delta t^2 (R\bar{T}/2) + i\bar{u} k_x \Delta t$. This results from a Fourier stability analysis of Eqs. (16) using the linearization

$$f^{n+1} = \bar{f}_0 + \frac{\partial \bar{f}_0}{\partial \bar{\rho}} \underset{\sim}{\rho}^n(x - ct) + \frac{\partial \bar{f}_0}{\partial \bar{u}} \underset{\sim}{u}^n(x - ct) + \frac{\partial \bar{f}_0}{\partial \bar{T}} \underset{\sim}{T}^n(x - ct)$$

in place of Eq. (17) and by neglecting higher order nonlinear terms. The eigenvalues of G are

$$\lambda^{(i)} = e^{-\xi} Q^{(i)},$$

where $Q^{(1)} = 1$ and $Q^{(2,3)}$ are the roots of

$$(1 - Q)^2 + \delta(1 - Q) - \delta = 0,$$

where

$$\delta = -a^2 k_x^2 \Delta t^2 + k_x^4 \Delta t^4 \frac{R^2 \bar{T}^2}{10}.$$

For $RTk_x^2 \Delta t^2$ in the ranges $[0, 4]$ and $[10, 14]$, $Q^{(2)}$ and $Q^{(3)}$ are complex conjugate. Therefore $Q\bar{Q}^{(2,3)} = Q^{(2)}Q^{(3)}$ and inspection of the quadratic shows that $Q^{(2)}Q^{(3)} = 1$. Hence

$$|\lambda^{(i)} \bar{\lambda}^{(i)}|^{1/2} = e^{-k_x^2 \Delta t^2 (R\bar{T}/2)} \leqslant 1.$$

For $RTk_x^2 \Delta t^2$ outside those ranges direct computation shows that the exponential dominates $Q^{(2)}$ and $Q^{(3)}$ such that the inequality is always satisfied. This shows that the method is unconditionally stable and that short wavelength Fourier components are damped in the method.

APPENDIX B: NOMENCLATURE

a	speed of sound
c	molecular velocity space coordinate
c_v	specific heat at constant volume
D	diffusion coefficient in Eq. (22)
e_i	molecular internal energy
E	total energy per unit mass
f	probability density of molecular velocities
f_0	Maxwellian equilibrium velocity distribution
G	amplification matrix
k	wave number
L	$2L + 1$ = number of grid points in molecular velocity space
M	Mach number

N	number of grid points in physical space
P	gas pressure
R	gas constant
t	time
T	temperature
u	gas velocity
U	Fourier amplitude function
x	physical space coordinate

Greek Symbols

α	constant in Chapman–Enskog correction, Eq. (23)
β	constant in diffusion coefficient, Eq. (22)
Δc	mesh spacing in molecular velocity space
Δt	numerical time step
Δx	mesh spacing in physical space
Θ	wave number $jk_x\Delta x$
λ	eigenvalue
ρ	gas density

Subscripts

B	moving boundary value
i	running index 1, 2, 3
j	running index $1,\ldots, N$
l	running index $-L,\ldots, 0,\ldots, L$
m	boundary value
x	physical space
$\sim$	fluctuating part

Superscripts

n	time level $n\Delta t = t$
—	average value, complex conjugate

ACKNOWLEDGMENTS

The author would like to thank Professors S. Burstein, H. Grad and E. Isaacson for helpful discussions and comments. This work was supported at the Courant Institute of Mathematical Sciences, New York University, under DOE Contract DE-AC02–76ER03077.

REFERENCES

1. D. I. PULLIN, *J. Comput. Phys.* **34** (1980), 231.
2. S. KANIEL AND J. FALCOVITZ, Approximation of the Hydrodynamic Equations by a Transport Process, *in* "Proceedings of IUTAM Symposium on Approximation Methods for Navier–Stokes Problems," Lecture Notes in Mathematics No. 771, p. 272, Springer-Verlag, Berlin/New York/Heidelberg, 1980.

3. W. G. VINCENTI AND C. H. KRUGER. "Introduction to Physical Gas Dynamics," Wiley, New York. 1967.
4. G. A. SOD, *J. Comput. Phys.* **27** (11978), 1.
5. H. W. LIEPMAN AND A. ROSHKO, "Elements of Gas Dynamics," 8th printing, Wiley, New York. 1967.
6. K. SRINIVAS, J. GURURAJA, AND K. KRISHNA PRASAD, *J. Comput. Phys.* **20** (1976), 140.